

**Serveur Académique Lausannois SERVAL [serval.unil.ch](http://serval.unil.ch)**

## **Author Manuscript**

**Faculty of Biology and Medicine Publication**

**This paper has been peer-reviewed but does not include the final publisher proof-corrections or journal pagination.**

Published in final edited form as:

**Title:** En face optical coherence tomography of foveal microstructure in full-thickness macular hole: a model to study perifoveal Müller cells.

**Authors:** Matet A, Savastano MC, Rispoli M, Bergin C, Moulin A, Crisanti P, Behar-Cohen F, Lumbroso B

**Journal:** American journal of ophthalmology

**Year:** 2015 Jun

**Volume:** 159

**Issue:** 6

**Pages:** 1142-1151.e3

**DOI:** 10.1016/j.ajo.2015.02.013

## Title page

En face optical coherence tomography of foveal microstructure in full-thickness macular hole: a model to study perifoveal Müller cells

## Authors:

Alexandre Matet<sup>1</sup>, Maria Cristina Savastano<sup>2,3</sup>, Marco Rispoli<sup>3,4</sup>, Ciara Bergin<sup>1</sup>, Alexandre Moulin<sup>1</sup>, Patricia Crisanti<sup>5</sup>, Francine Behar-Cohen<sup>1,5</sup>, Bruno Lumbroso<sup>3</sup>

<sup>1</sup> Department of ophthalmology, University of Lausanne. Jules-Gonin Eye Hospital. Fondation Asile des Aveugles, Lausanne, Switzerland

<sup>2</sup> Department of Ophthalmology, Catholic University of Rome, Rome, Italy

<sup>3</sup> Centro Italiano Macula, Rome, Italy

<sup>4</sup> Nuovo Regina Margherita Hospital, Rome, Italy

<sup>5</sup> Inserm, U1138, Team 17, From physiopathology of ocular diseases to clinical development, Université Paris Descartes Sorbonne Paris Cité, Centre de Recherche des Cordeliers, Paris, France

Corresponding author:

Francine Behar-Cohen  
Hôpital Ophtalmique Jules-Gonin  
Avenue de France 15  
CP 133  
1000 Lausanne 7  
Switzerland  
Tel: + 41-21 626 85 82  
Fax: +41-21 626 85 96  
francine.behar@gmail.com

Suggested short title: En face OCT of macular hole and perifoveal Müller cells

## INTRODUCTION

En-face optical coherence tomography (OCT) is an emerging imaging modality that facilitates the assessment of retinal structures transversely.<sup>1,2</sup> Available since 2006 on certain OCT devices, the first retinal transverse scans were difficult to analyze interpret as only plane sections of the concave retina were available.<sup>3</sup> More recently, Spectral-Domain OCT technology with advanced alignment algorithm have adjusted sections to a reference curve, which has allowed layer-by-layer retinal imaging and provided a new investigation tool for a range of retinal disorders.<sup>4-9</sup>

The foveal microstructure is formed by a dense compaction of cone photoreceptors and their projected axons, which are intertwined with retinal glial Müller cells and follow a centrifugal course towards the inner layers at the edges of the fovea. Retinal glial Müller cells are critical for retinal homeostasis, providing metabolic support to neighboring neural cells, delivering neuroactive substances and retinoids to cones, and recycling waste compounds.<sup>10,11</sup> Müller cells are 5 times more abundant in the macula than in the peripheral retina.<sup>12</sup> The “Z-shape” morphology of perifoveal Müller cells has been observed on histological sections in both animal and human models, where the cells adopt three consecutive orientations (Figure 1).<sup>13,14</sup> From the internal limiting membrane, perifoveal Müller cells run vertically to the inner nuclear layer, then turn inwards towards the foveal center across the outer plexiform layer and the Henle’s fiber layer where their course is oblique and almost horizontal in the internal portion of the foveal pit. Then, at the junction with the outer nuclear layer, they take a vertical orientation again to reach the external limiting membrane (Figure 1). At the external limiting membrane of the primate retina, Omri et al. have previously shown that Müller cells and photoreceptors are bound by tight-like junctions, where the proteins occludin and zonula occludens-1 are expressed.<sup>15</sup>

Intraretinal fluid accumulation disrupts the foveal architecture, presenting an opportunity to examine its components in better detail. In full-thickness macular hole (MH), intraretinal cysts are frequently observed on OCT around the edges of the hole. On fluorescein angiography, no vascular leakage or filling of the cysts is usually observed.<sup>16</sup> This suggests that they originate from a metabolic dysfunction and supports the hypothesis of Müller cells implication in the pathogenesis of full-thickness MH.<sup>17-19</sup>

In this study, we use en face OCT to characterize and quantify layer by layer, the perifoveal cystic cavities occurring around full-thickness MHs. To support the OCT findings, we used human and non-human primate macular flat-mounts and sections to visualize Müller cells stained with a glial marker.

## METHODS

### *Subjects*

This observational case series adhered to the tenets of the Declaration of Helsinki, and the need of approval was waived by the Institutional Review Board of the Nuovo Regina Margherita Hospital, due to its retrospective nature and the restriction of the analysis to retinal imaging. Eight eyes from 8 patients presenting with a full-thickness MH surrounded by cystoid cavities were retrospectively included,

and high-quality images were reviewed. These eyes had been imaged between May 2011 and June 2014 at the clinical practice Centro Italiano Macula, Rome, Italy. Cases with media opacities, or any other macular disorder than full-thickness MH (as epiretinal membrane, choroidal neovascularization, macular atrophy, macular edema of vascular, diabetic or inflammatory origin) were excluded. All patients had been evaluated with comprehensive ophthalmological examination including full medical history, best-corrected visual acuity testing, slit lamp biomicroscopy and funduscopy. After pupillary dilation, OCT imaging was performed using either the RTVue100 (Optovue, Fremont, CA, USA) or Spectralis (Heidelberg Engineering, Heidelberg, Germany). Full-thickness MH staging was based on Gass classification system.<sup>20</sup>

### *En face OCT acquisition*

Spectralis images of the macular cube of  $20^\circ \times 20^\circ$  (corresponding to approximately  $3.6 \text{ mm} \times 3.6 \text{ mm}$ ) composed of 145 fast horizontal B scans had been acquired, with the Automatic Real-Time mode averaging 2 images for each scan. Within the Spectralis device, the best-fitting segmentation was applied to all images, and the internal limiting membrane reference was preferred over the Bruch membrane reference for both inner and outer retinal layers, in order to compensate for the high angulation between the full-thickness MH edges and the plane of the Bruch membrane. The thickness of en face sections had been set to  $20 \mu\text{m}$ .

On the RTVue-100 device, OCT scans had been acquired using the “3D reference” protocol. 141 high-speed B scans were performed inside a  $7 \text{ mm} \times 7 \text{ mm}$  square area projected on the macula, without eye tracking. The total acquisition time was 4 seconds. For the segmentation of the resulting virtual macular cube, en face images of inner retinal sections were obtained using the internal limiting membrane as reference (except for one case where inner plexiform layer (IPL) was used), whereas sections of the outer retinal layers were obtained using the RPE as reference, in the “RPEfit” mode. The thickness of en face sections varied between  $19 \mu\text{m}$  and  $25 \mu\text{m}$ .

### *Scans selected for analysis*

Since hyporeflective cavities observed at the edges of full-thickness MHs were concentrated inside the inner nuclear layer and inside the complex formed by the outer plexiform and Henle’s fiber layers, en face OCT scans from these two regions were retained for analysis (Figure 2). For each layer, a scan with the highest possible quality was selected among those located centrally in the stack, and was used to measure the areas of hyporeflective spaces in the frontal plane.

### *Quantitative measure of cavities area*

In order to obtain comparable images between the RTVue-100 and the Spectralis, a TIFF image centered on the fovea corresponding to  $3.6 \times 3.6 \text{ mm}$  was extracted from the en face scans obtained with the two devices. These en face OCT scans were analyzed using Image J software (Version 1.48q, Wayne Rasband, National Institutes of Health, Bethesda, MD, USA). Briefly, after conversion to 8-bit grayscale images, hyporeflective spaces were identified via the built-in “Adjust

threshold” function (with grayscale intensity threshold set to 64). On the resulting binary images, all identified hyporeflective spaces were transformed to white areas on a black background. A list of surfaces was obtained using the base package particle analysis function. In order to reduce noise, surfaces greater than 0.001 mm<sup>2</sup> was set as the threshold for inclusion in particle analysis calculations. Two statistical analyses were then performed. First, the distributions of cavities areas in the inner nuclear layer and in the complex of the outer plexiform and Henle’s fiber layers were compared within each subject using a Mann-Whitney-Wilcoxon sum-rank test for non-normal distributions. Second, overall comparison of cavity areas between the inner nuclear layer and the complex of the outer plexiform and Henle’s fiber layers was performed by a Kruskal-Wallis test and a multiple comparison post-test. Statistical analyses were performed on R Software (Version 3.1.1, R Foundation for Statistical Computing, R Core Team, 2014, Vienna, Austria. <http://www.R-project.org/>) using the “ggplot2” package (H. Wickham. ggplot2: elegant graphics for data analysis. Springer New York, 2009) for graphical representations and the “pgirmess” package for post-tests (Version 1.5.9, Patrick Giraudoux, 2014, <http://CRAN.R-project.org/package=pgirmess>). P values inferior to 0.05 were considered statistically significant.

#### *Supportive evidence: Immunocytochemistry of human and non-human primate retina*

The use of animals adhered to the ARVO statement for Ophthalmic and Vision Research and protocols were approved by the ethics committee of the Paris Descartes University. Three eyes from three monkeys (*Macaca fascicularis*) were used. Animals were sacrificed by CO<sub>2</sub> inhalation for other purposes. One healthy human eye from a patient with high-grade mucoepidermoid carcinoma of the tarsal conjunctiva extending into the orbit and requiring orbital exenteration was obtained from the ocular pathology laboratory at Jules-Gonin Eye Hospital, in accordance with regulations of the Lausanne University Institutional Review Board.

Cross-sections of the human retina and one monkey retina were stained with anti-glutamine synthetase MAB 302 antibodies (Chemicon Technology, Merck Millipore, Billerica, MA, USA). Other sections from the primate retina were co-stained with anti-glutamine synthetase MAB 302 and anti-zonula occludens-1 antibodies (Santa Cruz Biotechnology Inc., Santa Cruz, CA, USA), and counterstained with 4',6-diamidino-2-phenylindole (DAPI) (Sigma Aldrich, St Louis, MO, USA). Two primate retinas were flat-mounted after either staining with anti-glutamine synthetase MAB 302 antibodies or co-staining with anti-glutamine synthetase MAB 302 antibodies and anti-zonula occludens-1 antibodies. Images were captured using fluorescence and confocal microscopes. (See Supplementary Appendix for the detailed protocol)

## RESULTS

### *En face OCT of parafoveal cystoid cavities*

Mean age of the eight included subjects (4 females, 4 males) was 69.3 ± 8.1 years. Two patients had Stage 2, two had Stage 3, and four had Stage 4 full-

thickness MH. When considering the eight cases together, the mean area of hyporeflective spaces was significantly lower in the inner nuclear layer than in the complex formed by the outer plexiform and the Henle's fiber layers ( $5.3 \times 10^{-3} \text{ mm}^2$  against  $15.9 \times 10^{-3} \text{ mm}^2$ ,  $P < 0.0001$ , Kruskal-Wallis test). As shown in Figure 3, the statistical distribution and mean value of cavities areas also differed within each subject, where significantly smaller cavities were observed in the inner nuclear layer than in the complex of the outer plexiform and the Henle's fiber layers (Mann-Whitney-Wilcoxon rank-sum test). Patient characteristics and area measures are reported in the Table. In Figure 3 and Figure 4 it is clear that the hyporeflective spaces also differed in shape: their aspect was rounded in the inner nuclear layer, while the cavities appeared elliptic and radially oriented in the complex of the outer plexiform and the Henle's fiber layers.

Examination of the stack of en face OCT sections within the inner nuclear layer, showed that most cavities could be followed along a vertical axis, an example of this is shown in Figure 5. Superimposition of neighboring consecutive sections demonstrated that these smaller, rounded hyporeflective spaces formed parallel vertical bundles. In addition, vertical elongation of hyporeflective cavities in the inner nuclear layer was visible on B-scans, although not always visualized entirely due to the lack of strict parallelism with the section plane (see Figure 2).

Figure 4 also showed that in the complex of the outer plexiform and the Henle's fiber layers the elongated hyporeflective spaces adopted a radial or "petalloid" pattern, delineated by thin hyperreflective walls. In addition, OCT B-scans indicated that these outer retinal cavities originated above the external limiting membrane and respected this hyperreflective band across the portion of the macula affected by morphologic changes around the full-thickness MH. The outermost region of the neurosensory retina encompassing the photoreceptor inner and outer segments was indeed devoid of hyporeflective cavities on B-scans (Figure 2). On en face scans, this region appeared as a homogenous hyperreflective ring forming the edges of the full-thickness MH that did not contain hyporeflective spaces (Figure 4).

#### *Morphologic analysis of Müller cells in human and primate maculae*

As in humans, Müller cells of the primate macula are extremely dense and follow a concentric distribution. This distribution was evident on a flat-mounted retina from a healthy monkey, labeled with glutamine synthetase, a specific marker of glial cells (Figure 6). A confocal photograph of the same flat-mounted retina at a higher magnification confirmed the presence of radial and horizontal orientation of the intermediate segments of Müller cells that travel parallel to the Henle fibers. Importantly single Müller cells remained visible across the perifovea following a stellate pattern (Figure 6). A second retina from a healthy primate was then co-labeled for glutamine synthetase and zonula occludens-1. On the flat-mounted macula from this monkey the tight packing of Müller cells (red) with cone extensions (Henle's fibers) and other Müller cells by zonula occludens-1 (green, and yellow when co-localized with glutamine synthetase) was visible (Figure 7, Top). The visualization of radial perifoveal distribution of Müller cells surrounded by zonula occludens-1 was possible under higher magnification (Figure 7, Bottom).

A macular section of a third healthy primate retina demonstrated again the “Z-shape” of Müller cells, and their dense packing inside the Henle’s fibers layer where they co-localized with zonula occludens-1 (Figure 7). This “Z-shaped” profile was also visible on histological sections of the first-mentioned retina after specific glial labeling for glutamine synthetase (Figure 6). From the external limiting membrane, the cells followed the previously described triple course with a short vertical segment, an intermediate long oblique portion and a final vertical segment terminating at the internal limiting membrane. Even though these Müller cells progressed in parallel and formed a bundle, it was possible to visualize them individually.

## DISCUSSION

In the present study, stacks of en face OCT images were used to characterize the perifoveal hyporeflective spaces observed around full-thickness MHs. These cavities were invariably located in the inner nuclear layer and in the complex of the outer plexiform and the Henle’s fiber layers, and had a specific morphology and distribution in each layer: 1) thin vertical cylinders in the inner nuclear layer and 2) large horizontal ellipsoid spaces in the complex of the outer plexiform and the Henle’s fiber layers. This finding was reproduced on eight subjects, with two different OCT devices, which is indicative that the changes in foveal microstructure associated with full-thickness MH formation share a common cellular factor. The characterization of these hyporeflective cavities corresponded well with the previously reported “Z-shape” and radial course of Müller cells, described here in primate and human maculae.

Intraretinal cystoid cavities at the edges of full-thickness MHs had been recognized by investigators using the early OCT prototypes.<sup>21</sup> These hyporeflective spaces were diversely called “cystoid changes”,<sup>21</sup> “cystoid spaces”,<sup>22</sup> or “intraretinal cavities”,<sup>23</sup> but their exact nature has not been elucidated. Regarding their localization, Ko et al. have previously identified the inner nuclear layer and “the interface between the outer nuclear layer and the outer plexiform layer” as the retinal layers that were mainly affected.<sup>24</sup> In this region, Scholda et al. described fine structures separating the cystoid spaces and identified them as Müller cells possibly bridging between the outer plexiform and the outer nuclear layers.<sup>22</sup> In lamellar holes, the term “wagon-wheel sign” has been recently proposed to describe a similar stellate aspect on en face OCT images.<sup>25</sup>

Previous histological observational studies with light and electron microscopy have described the Henle’s fiber layer as the external portion of the outer plexiform layer.<sup>26</sup> On conventional axial OCT scans it can be challenging to distinguish the change in reflectivity of the Henle’s fiber layer at its interface with the outer nuclear layer. However, when the entrance beam of the OCT is not on the optical axis and there is a tilt with the retinal surface the Henle’s fibers can be clearly resolved.<sup>27,28</sup> Consequently, the recent nomenclature of the “IN•OCT Consensus” included the Henle’s fiber layer among the normal anatomic landmarks seen on spectral-domain

OCT, based on the fact that a subtle demarcating transition between Henle's fiber layer and outer nuclear layer is actually visible on non-tilted scans.<sup>29</sup> In this article, we have referred to the "complex formed by the outer plexiform and the Henle's fiber layers" to describe the entity formed by these two layers.

A graphical interpretation of the orientation and shape of the cavities surrounding full-thickness MHs formulated in this article has been given in **Figure 4**. Within the complex of the outer plexiform and the Henle's fiber layers, their distribution is similar to the radial pattern of Müller cells observed on labeled retinal flat-mounts (Figure 4 vs Figure 6). Similarly, the aspect of vertical cavities within the inner nuclear layer correlates well with the vertical portion of Müller cells course across inner retinal layers. By correlating these imaging findings to flat-mounts of primate retina after specific glial labeling, we hypothesized that the "Z-shaped" configuration of Müller cells explains the dual pattern of cystoid cavities surrounding full-thickness MHs.

There are several hypotheses regarding the mechanisms of full-thickness MH formation. Gass proposed that a prefoveal vitreous cortex contraction exerting a tangential traction on the macula caused a split of the glial material located in the inner part of the foveal center, a key region he termed the "Müller cell cone" after Yamada and Hogan, ultimately leading to a full-thickness defect.<sup>17,26,30-32</sup> Subsequent observations based on ultrasound and OCT imaging suggested that a role may be played by anterior-posterior vitreomacular tractions and posterior vitreous detachment in the genesis of full-thickness MHs.<sup>23,33-35</sup> These theories acknowledged the primary role of the vitreomacular interface, composed by the junction between vitreous collagen fibrils and the internal limiting membrane, where glial Müller cells arborize to form their basal membrane. This is consistent with the observation by Ezra et al. of glial material from Müller cells in an immunocytochemical study of 12 macular hole opercula, with 6 of these opercula also harboring a significant amount of cone photoreceptors, suggesting a full-thickness avulsion of neuroretinal tissue.<sup>36</sup> It also explains the development of a central foveal cyst due to the splitting of the fovea during early stages of full-thickness MH formation,<sup>18</sup> and the beneficence of posterior vitreous cortex removal in the treatment of MHs.<sup>37</sup> The role of Müller cells in the maintenance of foveal architecture and their activation during MH formation is also illustrated by their contribution to the scarring process accompanying MHs, although it is still debated whether this fibroglial proliferation is a primary process causing the hole, or a secondary reaction.<sup>35</sup>

Indeed, an enlargement of the "Z-shaped" configuration of Müller cells inside the scaffolding of the macular microstructure would be consistent with the observations reported in this study. Large, oval, horizontal cavities in the complex of the outer plexiform and the Henle's fiber layers follow the radial distribution of Müller cells in these layers. Similarly, the aspect of vertical and cylindrical cavities within the inner nuclear layer correlates well with the vertical track of Müller cells as they transverse a higher density of nuclei, horizontal and vertical intercellular connections. Müller cells are indeed the only retinal cells whose course spans both affected regions, and whose histological configuration is compatible with the reported en face OCT images.

It is not yet understood whether these cavities result from fluid accumulation inside the Müller cells themselves, as previously described in various pathological conditions as diabetes, ischemia, and inflammation,<sup>10</sup> or within intercellular spaces structured by the framework of Henle fibers and Müller cells. Both mechanisms could lead to the particular distribution of cavities in full-thickness MH-associated edema as visualized by en face OCT. The microstructural separation of individual Müller cells observed on primate retinal flat-mounts (Figures 6 and 7) suggest that Müller cells have the ability to separate from each other in pathological conditions. Interestingly, the observation of positive zonula occludens-1 labeling between cone axons and Müller cells in the Henle's fiber layer could explain that Müller cell dysfunction would lead to the disruption of these junctions and allow for larger spacing between cells, visualized as the larger cavities observed in the complex of the outer plexiform and the Henle's fiber layers. In addition, the presence of excessive fluid in the intercellular spaces or inside the cells could result from a dysfunction of the hydro-ionic regulation of Müller cells. During the early stages of MH formation, the retinal stretching induced by the vitreomacular traction can indeed result in a reduction in interstitial fluid pressure, with subsequent influx of water, ions, and molecules from the retinal vasculature.<sup>38</sup> Müller cells activated to drain these accumulated extracellular products may enlarge as a result of excessive protein intake, creating an osmotic gradient that would retain intracellular water in excess. Eventually, after vitreomacular traction release and full-thickness MH formation, the metabolic functions of Müller cells may remain altered.

This study has several limitations. Here we have provided a methodology to analyze perifoveal cavities around full-thickness MHs, however we have reported these results in a limited number of eyes, and no assessment of visual function or evolution of pathological features over time has been made. Future studies may investigate whether these cavities progress over time and whether their characteristics are related to the disease stage. Furthermore, although we observed the "Z-shaped" course of perifoveal Müller cells in cross-sections of one human retina, the flat-mounts used to investigate their histology were of primate origin, which needs to be repeated in human eyes. To the best of our knowledge, we are unaware of previous reports achieving the surface quantification of perifoveal cysts surrounding full-thickness MHs on en face OCT, and comparing these observations to the histology of the macula, and could find no reference to it in a computerized search on PubMed.

To summarize, en face OCT of perifoveal cysts in full-thickness MH and histology of flat mounted retinas showed a marked concordance, which is best explained by the paramount contribution of Müller cells to macular microstructure. Their radial and "Z-shaped" track from the outer to the inner retinal layers would explain both the stellar pattern of outer cystoid cavities, and the inner microcystic changes surrounding MHs. Histological ultrastructural studies, and en face OCT analysis of cystoid cavities in other macular disorders are needed to verify these findings.

## ACKNOWLEDGEMENTS

A. Funding/Support: none

B. Financial disclosures:

Matet: meeting expenses (Laboratoires Alcon S.A.S., Rueil-Malmaison, France; Laboratoires Théa, Clermont-Ferrand, France)

Savastano: no financial disclosures

Rispoli: no financial disclosures

Bergin: no financial disclosures

Moulin: no financial disclosures

Lassiaz: no financial disclosures

Behar-Cohen: no financial disclosures

Lumbroso: consultant (Optovue, Fremont, CA)

C. Author contribution:

- Design (BL, FBC) and conduct of the study (PC, MCS, MR, AMa, AMo, CB)
- Collection of data (MCS, MR, BL, AMo, PC, FBC, AMa, CB)
- Management (MR, MCS, AMo), analysis (AMa, CB), and interpretation (BL, FBC, PC) of the data
- Preparation (AMa, MCS, CB), review (PC, FBC, BL) and approval of the manuscript (AMa, MCS, MR, CB, AMo, PC, FBC, BL)

Each author meets the 4 criteria set by the International Committee of Medical Journal Editors (ICMJE) required to claim authorship.

D. Other acknowledgements:

Mehrad Hamedani (Jules-Gonin Eye Hospital, Lausanne, Switzerland) who provided the human donor eye.

## REFERENCES

1. Rosen RB, Hathaway M, Rogers J, et al. Simultaneous OCT/SLO/ICG imaging. *Invest Ophthalmol Vis Sci.* 2009;50(2):851-860.
2. Rosen RB, Hathaway M, Rogers J, et al. Multidimensional en-face OCT imaging of the retina. *Opt Express.* 2009;17(5):4112-4133.
3. Van Velthoven MEJ, Verbraak FD, Yannuzzi LA, Rosen RB, Podoleanu AGH, de Smet MD. Imaging the retina by en face optical coherence tomography. *Retina.* 2006;26(2):129-136.
4. Alkabes M, Salinas C, Vitale L, Burés-Jelstrup A, Nucci P, Mateo C. En face optical coherence tomography of inner retinal defects after internal limiting membrane peeling for idiopathic macular hole. *Invest Ophthalmol Vis Sci.* 2011;52(11):8349-8355.
5. Sallo FB, Peto T, Egan C, et al. "En face" OCT imaging of the IS/OS junction line in type 2 idiopathic macular telangiectasia. *Invest Ophthalmol Vis Sci.* 2012;53(10):6145-6152.
6. Nunes RP, Gregori G, Yehoshua Z, et al. Predicting the progression of geographic atrophy in age-related macular degeneration with SD-OCT en face imaging of the outer retina. *Ophthalmic Surg Lasers Imaging Retina.* 2013;44(4):344-359.
7. Pelosini L, Hull CC, Boyce JF, McHugh D, Stanford MR, Marshall J. Optical coherence tomography may be used to predict visual acuity in patients with macular edema. *Invest Ophthalmol Vis Sci.* 2011;52(5):2741-2748.
8. Gaudric A, Aloulou Y, Tadayoni R, Massin P. Macular pseudoholes with lamellar cleavage of their edge remain pseudoholes. *Am J Ophthalmol.* 2013;155(4):733-742, 742.e1-e4.
9. Sohrab M, Wu K, Fawzi AA. A pilot study of morphometric analysis of choroidal vasculature in vivo, using en face optical coherence tomography. *PLoS ONE.* 2012;7(11):e48631.
10. Bringmann A, Pannicke T, Grosche J, et al. Müller cells in the healthy and diseased retina. *Prog Retin Eye Res.* 2006;25(4):397-424.
11. Reichenbach A, Bringmann A. New functions of Müller cells. *Glia.* 2013;61(5):651-678.
12. Distler C, Dreher Z. Glia cells of the monkey retina--II. Müller cells. *Vision Res.* 1996;36(16):2381-2394.
13. Ramon y Cajal S. *Structure of the Retina.* C.C. Thomas; 1972.
14. Bringmann A, Reichenbach A, Wiedemann P. Pathomechanisms of cystoid macular edema. *Ophthalmic Res.* 2004;36(5):241-249.
15. Omri S, Omri B, Savoldelli M, et al. The outer limiting membrane (OLM) revisited: clinical implications. *Clin Ophthalmol.* 2010;4:183-195.
16. Agarwal A. *Gass's Atlas of Macular Diseases.* 5th ed. Elsevier; 2012.
17. Gass JD. Müller cell cone, an overlooked part of the anatomy of the fovea centralis: hypotheses concerning its role in the pathogenesis of macular hole and foveomacular retinoschisis. *Arch Ophthalmol.* 1999;117(6):821-823.

18. Haouchine B, Massin P, Gaudric A. Foveal pseudocyst as the first step in macular hole formation: a prospective study by optical coherence tomography. *Ophthalmology*. 2001;108(1):15-22.
19. Sugiyama T, Katsumura K, Nakamura K, et al. Effects of chymase on the macular region in monkeys and porcine muller cells: probable involvement of chymase in the onset of idiopathic macular holes. *Ophthalmic Res*. 2006;38(4):201-208.
20. Gass JD. Idiopathic senile macular hole. Its early stages and pathogenesis. *Arch Ophthalmol*. 1988;106(5):629-639.
21. Hee MR, Puliafito CA, Wong C, et al. Optical coherence tomography of macular holes. *Ophthalmology*. 1995;102(5):748-756.
22. Scholda C, Wirtitsch M, Hermann B, et al. Ultrahigh resolution optical coherence tomography of macular holes. *Retina*. 2006;26(9):1034-1041.
23. Gaudric A, Haouchine B, Massin P, Paques M, Blain P, Erginay A. Macular hole formation: new data provided by optical coherence tomography. *Arch Ophthalmol*. 1999;117(6):744-751.
24. Ko TH, Fujimoto JG, Duker JS, et al. Comparison of ultrahigh- and standard-resolution optical coherence tomography for imaging macular hole pathology and repair. *Ophthalmology*. 2004;111(11):2033-2043.
25. Clamp MF, Wilkes G, Leis LS, et al. En face spectral domain optical coherence tomography analysis of lamellar macular holes. *Retina*. 2014;34(7):1360-1366.
26. Hogan MJ, Alvarado JA, Weddel JE. *Histology of the Human Eye*. Philadelphia: W.B. Saunders Company; 1971.
27. Lujan BJ, Roorda A, Knighton RW, Carroll J. Revealing Henle's fiber layer using spectral domain optical coherence tomography. *Invest Ophthalmol Vis Sci*. 2011;52(3):1486-1492.
28. Otani T, Yamaguchi Y, Kishi S. Improved visualization of Henle fiber layer by changing the measurement beam angle on optical coherence tomography. *Retina*. 2011;31(3):497-501.
29. Staurengi G, Sadda S, Chakravarthy U, Spaide RF, International Nomenclature for Optical Coherence Tomography (IN•OCT) Panel. Proposed Lexicon for Anatomic Landmarks in Normal Posterior Segment Spectral-Domain Optical Coherence Tomography: The IN•OCT Consensus. *Ophthalmology*. 2014;121(8):1572-1578.
30. Yamada E. Some structural features of the fovea centralis in the human retina. *Arch Ophthalmol*. 1969;82(2):151-159.
31. Johnson RN, Gass JD. Idiopathic macular holes. Observations, stages of formation, and implications for surgical intervention. *Ophthalmology*. 1988;95(7):917-924.
32. Gass JD. Reappraisal of biomicroscopic classification of stages of development of a macular hole. *Am J Ophthalmol*. 1995;119(6):752-759.
33. Johnson MW, Van Newkirk MR, Meyer KA. Perifoveal vitreous detachment is the primary pathogenic event in idiopathic macular hole formation. *Arch Ophthalmol*. 2001;119(2):215-222.

34. Van Newkirk MR, Johnson MW, Hughes JR, Meyer KA, Byrne SF. B-scan ultrasonographic findings in the stages of idiopathic macular hole. *Trans Am Ophthalmol Soc.* 2000;98:163-171.
35. Smiddy WE, Flynn HW Jr. Pathogenesis of macular holes and therapeutic implications. *Am J Ophthalmol.* 2004;137(3):525-537.
36. Ezra E, Fariss RN, Possin DE, et al. Immunocytochemical characterization of macular hole opercula. *Arch Ophthalmol.* 2001;119(2):223-231.
37. Spaide RF. Closure of an outer lamellar macular hole by vitrectomy: hypothesis for one mechanism of macular hole formation. *Retina.* 2000;20(6):587-590.
38. Simpson ARH, Petrarca R, Jackson TL. Vitreomacular adhesion and neovascular age-related macular degeneration. *Surv Ophthalmol.* 2012;57(6):498-509.

## FIGURE CAPTIONS:

FIGURE 1. The "Z-shaped" course of perifoveal Müller cells in human and monkey retina.

(Left) Section of a normal human macula after labeling for glutamine synthetase, a marker of glial cells, showing the typical "Z-shaped" course of Müller cells.

(Right) Golgi-stained section of a monkey macula (*Macaca fascicularis*) with attribution of retinal layers, also displaying the "Z-shaped" morphology of Müller cells, which can be followed from external limiting membrane to internal limiting membrane. Müller cells nuclei are located in the Inner Nuclear Layer. (Adapted from Heinz Wässle, Frankfurt, Germany, with permission)

ILM: internal limiting membrane; RNFL: retinal nerve fiber layer; GCL: ganglion cell layer; IPL: inner plexiform layer; INL: inner nuclear layer; OPL: outer plexiform layer; HFL: Henle's fiber layer; ONL: outer nuclear layer; ELM: external limiting membrane

FIGURE 2. Localization of cystoid cavities around a full-thickness macular hole in the inner nuclear layer and in the complex of the outer plexiform/Henle fibers layer.

(Top) Horizontal Spectral-Domain OCT B-scan of a normal macula with manual segmentation of retinal layers. A faint demarcation between the Henle fibers layer and the outer nuclear layer is visible.

(Bottom) Horizontal Spectral-Domain OCT B-scan of a full-thickness macular hole (Case 6) with manual segmentation of retinal layers showing the specific localization of perifoveal cystoid cavities in the inner nuclear layer and in the outer plexiform layer/Henle fibers layer complex.

RNFL: retinal nerve fiber layer; GCL: ganglion cell layer; IPL: inner plexiform layer; INL: inner nuclear layer; OPL: outer plexiform layer; HFL: Henle's fiber layer; ONL: outer nuclear layer.

FIGURE 3. Automated identification and surface quantification of hyporeflective spaces in the inner nuclear layer and the complex formed by the outer plexiform and Henle fibers layers on en face optical coherence tomography.

For each subject, findings are divided into two subcolumns: Inner Nuclear Layer and Outer Plexiform/Henle Fiber Layers complex. Each subcolumn includes: (Top) B-scan OCT indicating the plane of en face section; (Middle top) En face OCT showing the distinct patterns of hyporeflective spaces in the inner nuclear layer and the complex of the outer plexiform and the Henle's fiber layers; (Middle bottom) En face OCT displaying the detected hyporeflective areas (red); (Bottom) Boxplot graph showing the surface distribution of identified areas in the INL and the complex of the outer plexiform and the Henle's fiber layers. Centerline and diamond indicate the median and mean for each distribution, respectively. Boxes extend from the 1<sup>st</sup> to the 3<sup>rd</sup> quartile and vertical bars to the lowest and highest value within 1.5 interquartile range. For graphical convenience,

outliers were not displayed. Within each subject, the distribution of measured areas differed significantly between the two layers (\*=P<0.001, Mann-Whitney-Wilcoxon test). INL: inner nuclear layer; OPL: outer plexiform layer; HFL: Henle's fiber layer

FIGURE 4. En face optical coherence tomography imaging and schematic representation of perifoveal cavities around a full-thickness macular hole.

(Top and bottom left) En face OCT of a Stage 4 macular hole (Case 6) and (Top and Bottom middle) corresponding tridimensional display at the levels of the inner nuclear layer and the outer plexiform/Henle's fiber layers complex. Small, circular and evenly distributed hyporeflective spaces are visualized around the hole in the inner nuclear layer, and elongated radial hyporeflective cavities forming a stellar pattern are visualized in the outer plexiform/Henle's fiber layers complex. The hyperreflective ring at the edges of the hole corresponds to the outer nuclear layer and photoreceptor segments, where no cystoid spaces are observed.

Schematic representation of cystoid cavities around a full-thickness macular hole: (Top right) Rounded microcystic spaces identified in the INL correspond to horizontal sections of vertical cylindrical cavities; (Bottom right) In the complex of the outer plexiform and the Henle's fiber layers, the larger and stretched-out hyporeflective spaces correspond to sections of radial petalloid cavities around the fovea. Assuming that these cavities are connected to the vertical cylinders located in the INL, this suggests that "Z-shaped" Müller cells are a key contributor to the pathological changes of the foveal microstructure.

FIGURE 5. Stack of three non-overlapping en face optical coherence tomography scans of a full-thickness macular hole (Case 1) at the level of the inner nuclear layer showing the continuity of hyporeflective cavities.

The superposition of hyporeflective spaces reflects the cylindrical nature of the cavities. The green and yellow arrows indicate examples of hyporeflective spaces that can be followed along the 3 sections. ILM: internal limiting membrane

FIGURE 6. Flat-mounted primate macula viewed by fluorescence microscopy.

(Top left) Glial labeling for glutamine synthetase (GS, red) reveals a stellar pattern of fibers that corresponds to Müller cells radiating from the foveal center. In the perifoveal region, this distribution is replaced by diffuse dots suggesting a change to a vertical orientation, with a transition zone where both patterns coexist.

(Top right) A confocal image after glutamine synthetase-labeling (red) at higher magnification brings additional evidence of Müller cells "Z-shaped" pattern by showing that individual glial cells can be followed along their intermediate horizontal portion but are lost both at the foveal center and the peripheral fovea.

(Bottom) Histological section in the perifoveal region of a macaque retina after glial labeling by glutamine synthetase (red): the dotted white line indicates the characteristic “Z-shaped” track followed by Müller cells.

ILM: internal limiting membrane; OPL: outer plexiform layer; ELM: external limiting membrane GS: glutamine synthetase; DAPI: 4',6-diamidino-2-phenylindole

FIGURE 7. Primate macula viewed by fluorescence microscopy after staining for glutamine synthetase (red), zonula occludens-1 (green) and nuclei by **DAPI** (blue).

(Top left) Co-localization of glutamine synthetase and zonula occludens-1 labeling (yellow) along the radial arrangement of Henle fibers indicates a close anatomical relation between Müller cells and tight-junctions, probably located on the cone axons that compose the Henle fibers.

(Top right) This co-localization is better visualized on a magnified area.

(Bottom) A macular section confirms this co-localization along the horizontal course of Müller cells inside the Henle fibers layer. As expected, zonula occludens-1 is also expressed in the photoreceptors outer segments.

HFL: Henle's fiber layer; ONL: outer nuclear layer; ELM: external limiting membrane; OS: photoreceptors outer segments; GS: glutamine synthetase; ZO-1: zonula occludens -1; DAPI: 4',6-diamidino-2-phenylindole

### **New FIGURE 6**

Fluorescence microscopy of stained flat-mounted and sectioned primate macula analyzing the “Z-shaped” course of Müller cells in relation to adjacent cellular structures.

TABLE. Clinical and imaging characteristics of 8 patients presenting a full-thickness macular hole.

| Subject       | Age (years) | Gender | OCT device | Macular hole diameter ( $\mu\text{m}$ ) | Posterior vitreous detachment | Macular hole stage | Mean cavity area ( $\times 10^{-3} \text{ mm}^2$ ) |  | P value        |
|---------------|-------------|--------|------------|---|-------------------------------|--------------------|--|--|----------------|
|               |             |        |            |   |                               |                    | Inner nuclear layer                                | Outer plexiform / Henle's fiber layers |                |
| <b>Case 1</b> | 69          | F      | RTVue      | 673                                     | No                            | 3                  | 6.4  | 21.8                                   | $P < 0.0001^a$ |
| <b>Case 2</b> | 71          | F      | RTVue      | 787                                     | No                            | 3                  | 5.2  | 13.1                                   | $P = 0.0003^a$ |
| <b>Case 3</b> | 57          | F      | RTVue      | 560                                     | Yes                           | 4                  | 5.9  | 20.5                                   | $P < 0.0001^a$ |
| <b>Case 4</b> | 62          | F      | RTVue      | 350                                     | No                            | 2                  | 3.6  | 27.5                                   | $P = 0.0005^a$ |
| <b>Case 5</b> | 80          | M      | RTVue      | 385                                     | Yes                           | 4                  | 8.2  | 23.8                                   | $P < 0.0001^a$ |
| <b>Case 6</b> | 63          | M      | Spectralis | 556                                     | Yes                           | 4                  | 2.5  | 15.1                                   | $P < 0.0001^a$ |
| <b>Case 7</b> | 74          | M      | Spectralis | 341                                     | No                            | 2                  | 4.3  | 10.9                                   | $P < 0.0001^a$ |
| <b>Case 8</b> | 78          | M      | Spectralis | 238                                     | Yes                           | 4                  | 4.3  | 9.1                                    | $P < 0.0001^a$ |
| <b>Mean</b>   | 69.3        | -      | -          | 486                                     | -                             | -                  | 5.0  | 15.9                                   | $P < 0.0001^b$ |

OCT: optical coherence tomography

a. Mann-Whitney-Wilcoxon sum-rank test.

b. Kruskal-Wallis test with multiple comparisons post-test.

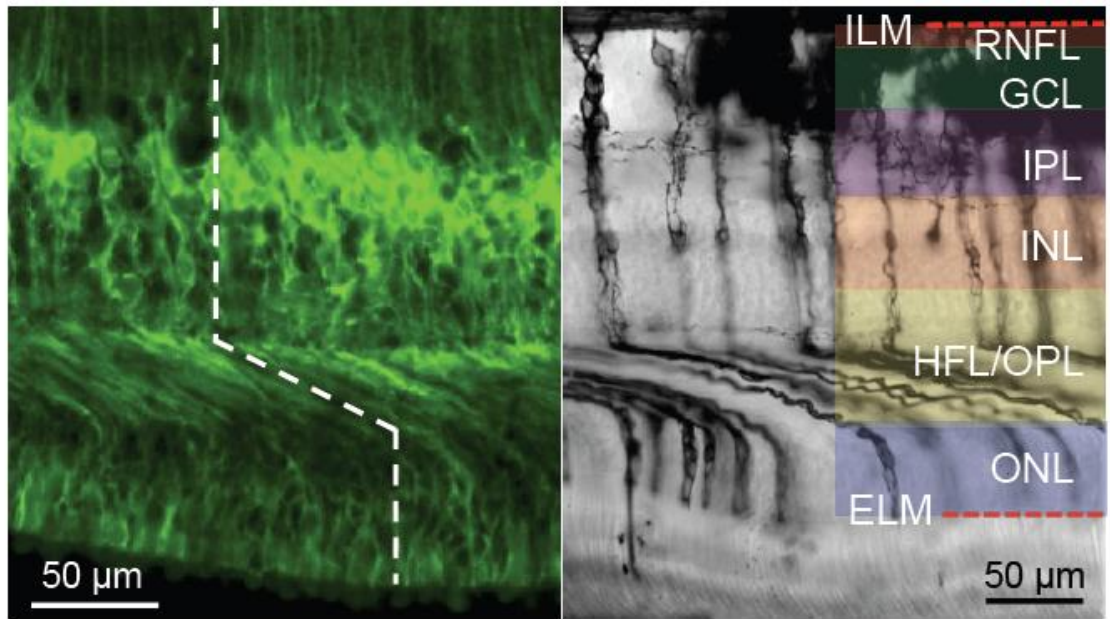


Figure 1

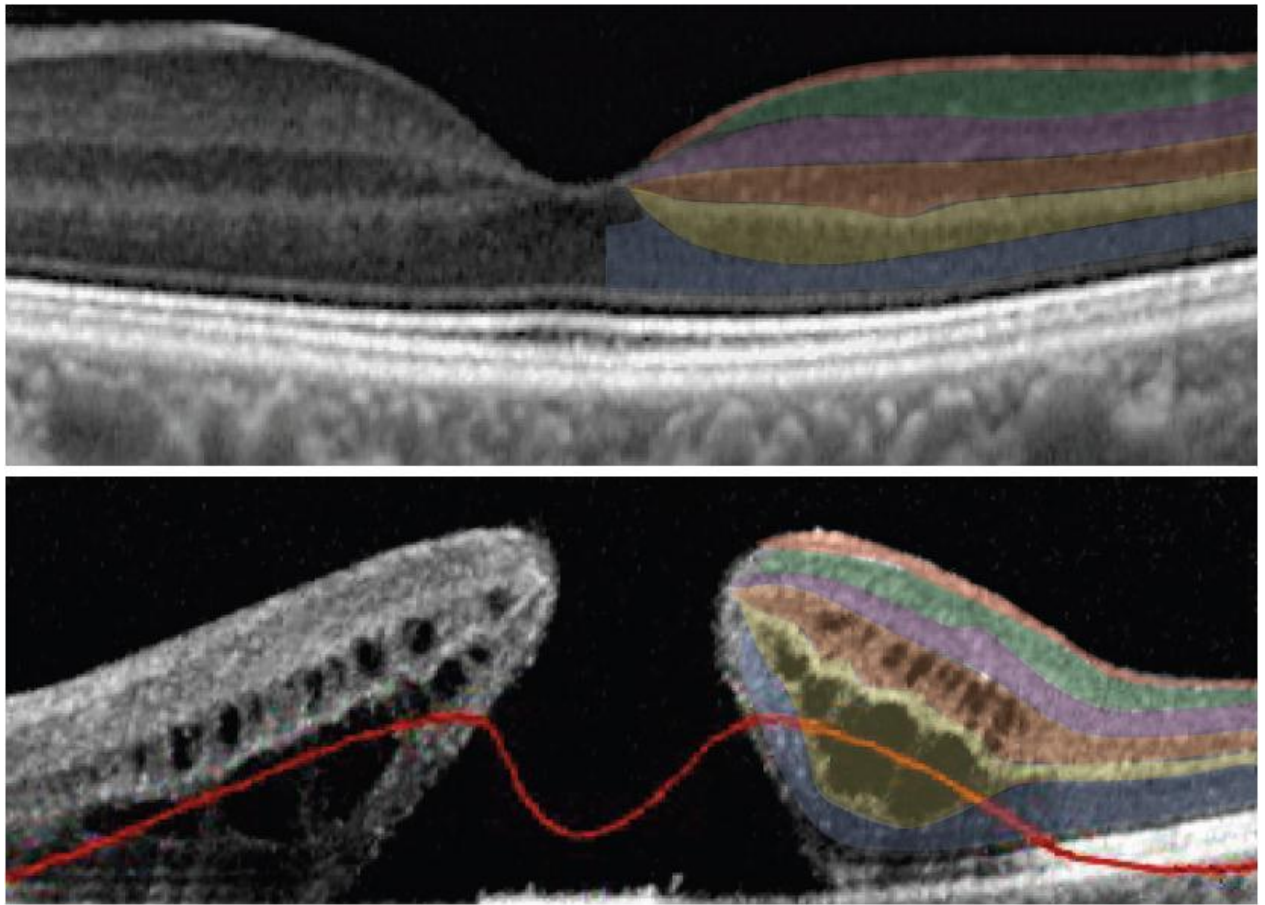


Figure 2

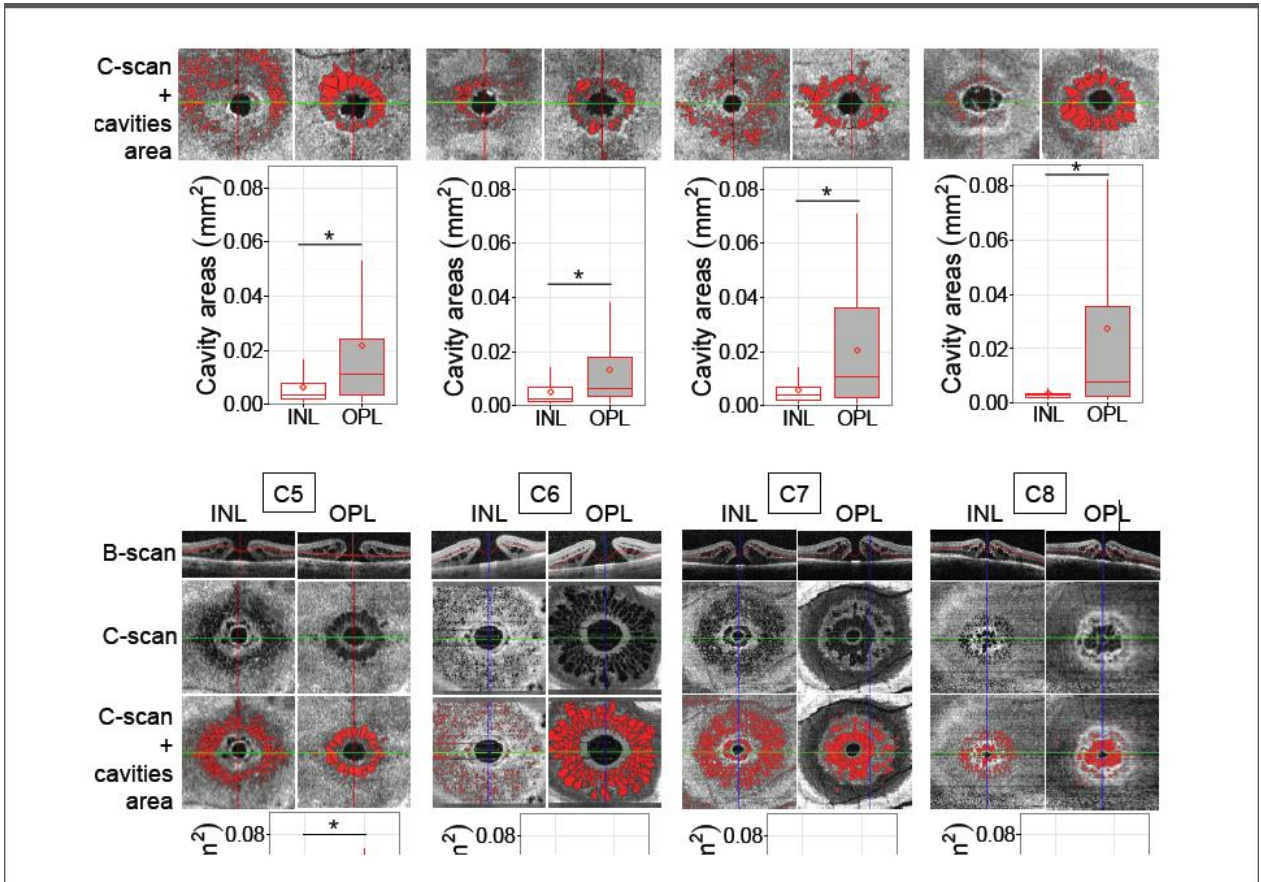


Figure 3

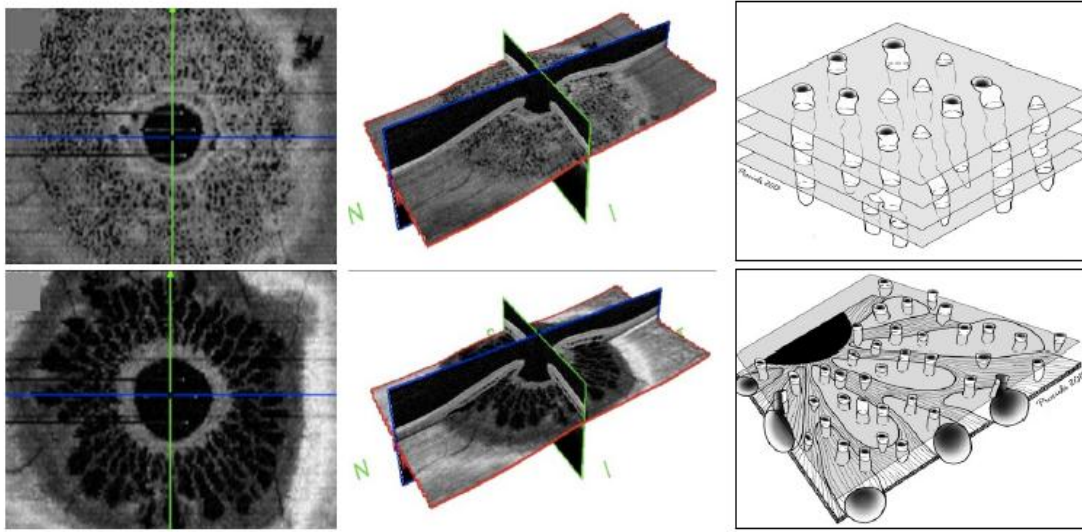


Figure 4

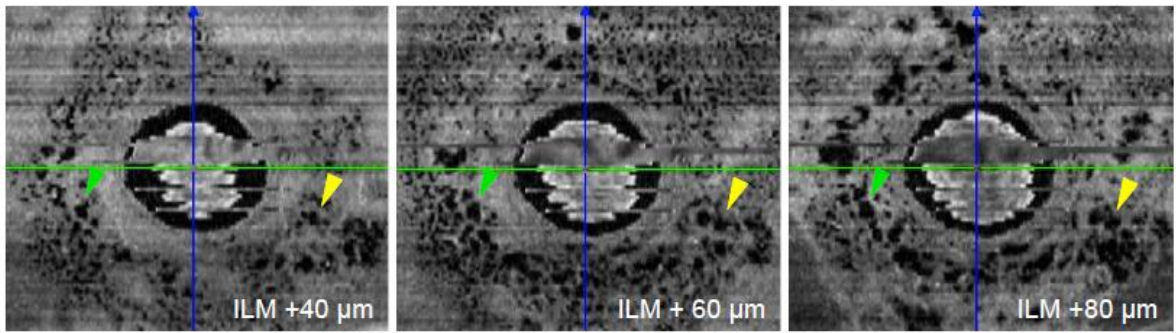


Figure 5

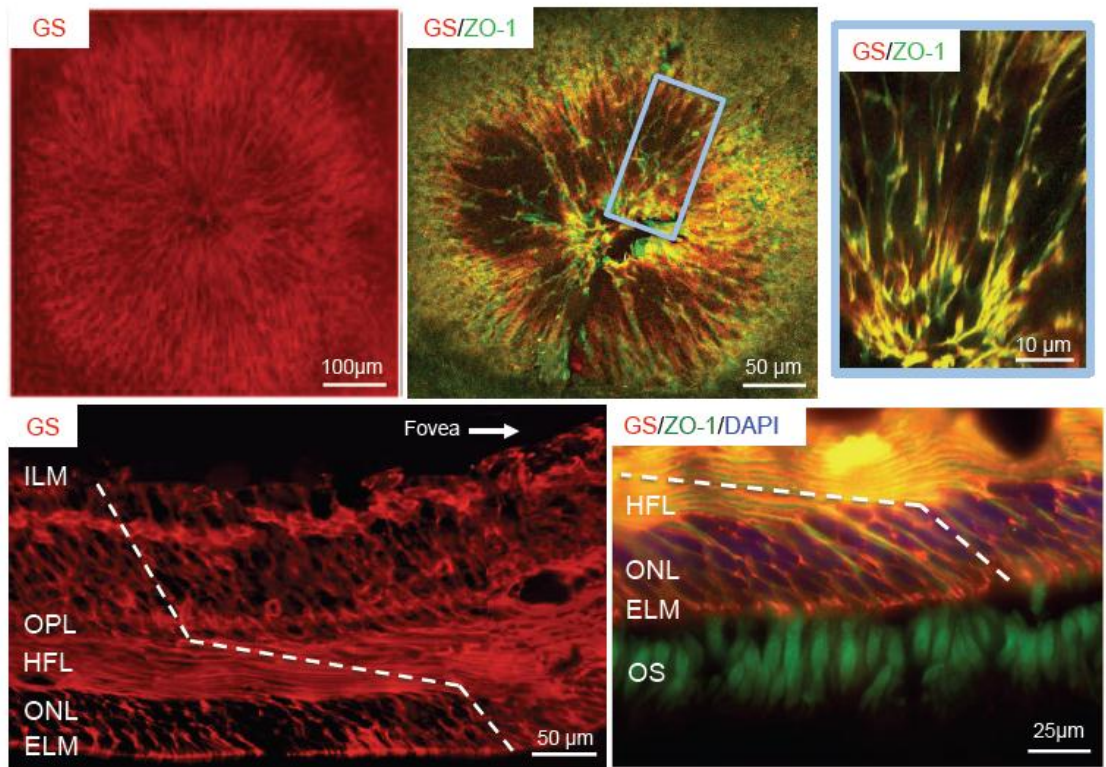


Figure 6